nature geoscience

ARTICLES

https://doi.org/10.1038/s41561-021-00871-5

Internal structure of ultralow-velocity zones consistent with origin from a basal magma ocean

Surya Pachhai[1,2]✉, Mingming Li[3], Michael S. Thorne[2], Jan Dettmer[4] and Hrvoje Tkalčić[1]

Seismological observations reveal patches of low-velocity anomalies at the core–mantle boundary known as ultralow-velocity zones. Despite recent advances, their origin and dynamic link to the lowermost mantle remain unclear. Here we employ seismic data analysis and high-resolution geodynamic modelling to study the origin of ultralow-velocity zones beneath the Coral Sea between Australia and New Zealand. The analysis of core-reflected waveforms with rigorous estimation of Bayesian uncertainties shows strong evidence of stratified density increases (~30%) and shear-wave velocity decreases (~50%) within the ultralow-velocity zones. These zones thin on two sides and occur at the edge of the Pacific large low-shear-velocity province. Geodynamic modelling demonstrates that these features are consistent with the presence of compositional heterogeneities within the ultralow-velocity zones that may be caused by the remnants of Earth's early differentiation. We conclude that small-scale structures that are compositionally distinct from their surroundings reside at the bottom of the mantle without full homogenization, throughout Earth's history.

Seismological studies of long-period shear waves reveal large low-shear-velocity provinces (LLSVPs) centred beneath the central Pacific and Africa that are surrounded by relatively high seismic velocities[1,2]. Analyses of seismic waveforms reveal small-scale structures above the core–mantle boundary (CMB) with shear (S)-wave velocity decreases of up to 50%, compressional (P)-wave velocity decreases of up to 25% and density increases up to 30% relative to the ambient mantle[3]. These structures are termed ultralow-velocity zones (ULVZs) and their properties were first quantified using forward waveform modelling of core-diffracted phases[4–6].

Seismic velocities and the origin of ULVZs

ULVZs were initially hypothesized to be due to partial melting based on a 3:1 ratio of their S- to P-wave velocity perturbations and a correlation between ULVZ locations and surface hotspots[7–9]. ULVZs have also been argued to be rooted at the base of major hot spot plumes and interpreted to be partially molten, particularly beneath Iceland[10]. However, ULVZs are also detected in high-velocity regions of the lowermost mantle[11,12], where temperatures are expected to be far lower than within LLSVPs. In addition, partial melting alone may not be able to explain ULVZs with positive density anomalies of more than 10% and smaller than a 3:1 ratio of the S- to P-velocity reductions[13,14].

Alternatively, compositionally distinct materials with increased intrinsic density can cause ULVZs. Geodynamic modelling shows that compositionally distinct ULVZs preferentially congregate at the edges of LLSVPs, although they may also temporally locate within and outside the LLSVPs[15,16], which is consistent with seismic observations. However, the origin of compositional heterogeneities in Earth's lowermost mantle remains unclear and current hypotheses include remnants of Earth's early differentiation[17], products of core–mantle reaction[18,19], and subducted materials[20,21]. It is critical to understand which of these hypotheses is most plausible, because each of them is linked to a specific path or event in Earth's evolution.

To improve our understanding of ULVZ origin, we present results from new seismic observations that sample the CMB beneath the Coral Sea between Australia and New Zealand, where observations of core-reflected seismic phases are abundant due to the high volume of earthquakes in the west-Pacific subduction zones and recording stations in Australia (Fig. 1). With high-resolution geodynamic modelling experiments, we provide a new understanding of the origin and dynamics of fine-scale structures within ULVZs.

Internal structure of ULVZs

Most previous studies assumed single-layer ULVZs and sought to constrain the thickness, P- and S-wave velocities and density obtained for that layer. Wherever possible, the ULVZ lateral extent was also estimated[8,22,23]. Some studies have also identified a multi-layer ULVZ structure[13,24,25]. However, substantial challenges exist when inferring the complex ULVZ structure, including (1) difficulties in identifying the converted phases for multiple layers and (2) difficulties in objectively choosing the model complexity. Models that are too complex can overfit the data, resulting in overestimated uncertainties, and models that are too simple may underfit the data, resulting in underestimated uncertainties. To address these issues, here we apply a nonlinear trans-dimensional Bayesian waveform inversion[24,25]. This method reduces subjectivity by treating the number of layers and noise parameters as unknown and satisfies model parsimony by favouring simple models consistent with the data. In this approach, parameter uncertainties are quantified by their posterior probability density (PPD). The PPD combines the prior information with data information, which is represented by the likelihood function. Here, prior ranges for ULVZ thickness, velocity and density are set based on previous studies. As waveform inversion is a highly nonlinear problem, a sampling approach is applied to compute the PPD. In particular, we apply a reversible jump Markov chain Monte Carlo sampling approach in which three different moves are proposed: addition of a new layer (birth), deletion of an existing layer (death) and change of only the layer properties (perturbation). Each of these

[1]Research School of Earth Sciences, The Australian National University, Canberra, Australian Capital Territory, Australia. [2]Department of Geology and Geophysics, University of Utah, Salt Lake City, UT, USA. [3]School of Earth and Space Exploration, Arizona State University, Tempe, AZ, USA. [4]Department of Geoscience, University of Calgary, Calgary, Alberta, Canada. ✉e-mail: surya.pachhai@utah.edu

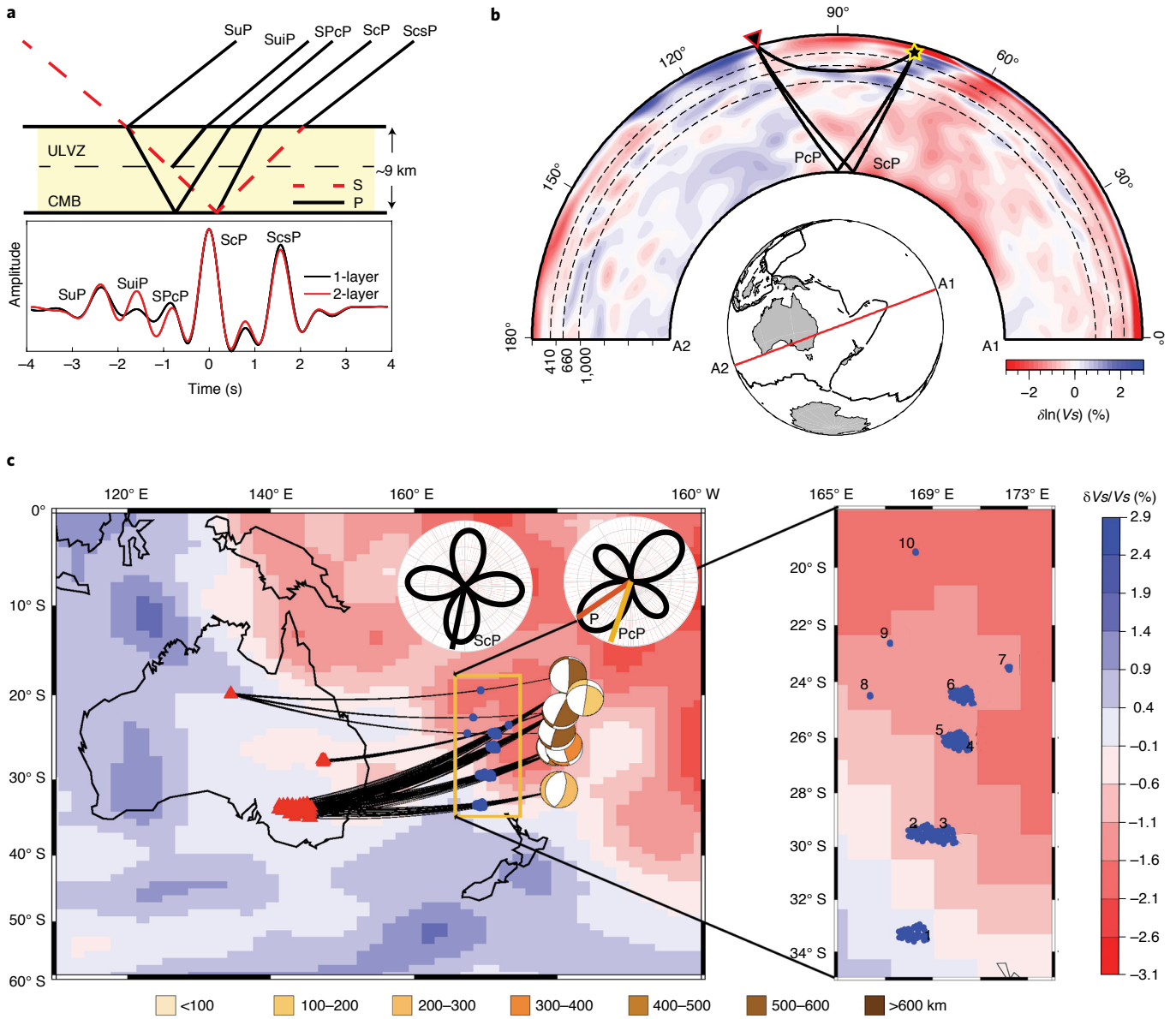

Fig. 1 | Illustration of data type and study region. a, ScP wave conversions and synthetic waveforms for one- and two-layer ULVZs. For simplicity, only a single conversion with noticeable amplitude (SuiP) is shown in the case of the two-layer ULVZ. **b**, P, PcP and ScP ray paths through the vertical cross-section of a global S-wave tomographic image[2] along the source (star) and receiver (inverted triangle) azimuth (path A1–A2 in the inset). **c**, Earthquake focal mechanisms (symbol colour represents depth), stations (triangles) and ray paths with sampling points (blue patches) at the CMB. Insets show radiation patterns and the take-off angles of the P, PcP and ScP waves. Numbered geographical bins are also shown.

moves is generated randomly and is accepted or rejected based on a probabilistic criterion (Methods).

With the Bayesian method we identified several regions beneath the Coral Sea that have waveforms consistent with ULVZs. A large number of deep-focus earthquakes in the Tonga-Fiji region and high-quality recordings on seismic arrays in Australia (Fig. 1c, Extended Data Figs. 1 and 2 and Supplementary Table 1) allow us to study a wide region of the lowermost mantle. Data from deep events avoid source-side upper-mantle S-wave attenuation and produce ScP waves (S waves reflected and converted to P waves from the CMB) with higher amplitudes. Furthermore, the ScP waveforms also show no effect of attenuation associated with the deep mantle and CMB topography (Methods). Unlike core-diffracted waves, ScP waves are directly sensitive to the internal structure of ULVZs (Fig. 1a) due to additional arrivals resulting from conversions (Fig. 1a) and have unique sampling at the CMB (Fig. 1b). For simplicity, only a single conversion with noticeable amplitude (SuiP) is shown in the case of the two-layer ULVZ in Fig. 1a. Because the S velocity on both layers is similar, the postcursor position remains unchanged. The exceptional data, combined with our novel statistical analysis, provide unprecedented resolution of the ULVZ internal structure. Note that this method requires many thousands of forward computations to achieve convergence. Our analysis uses highly efficient one-dimensional (1D) ray theory-based forward computation[26], which allows the evaluation of thousands of forward computations to quantify uncertainty. Although 2D and 3D forward calculations are sometimes considered, we have carefully chosen data that can be analysed under the assumption of a 1D forward model. To demonstrate that unbiased ULVZ estimates are obtained with our 1D method, we carried out

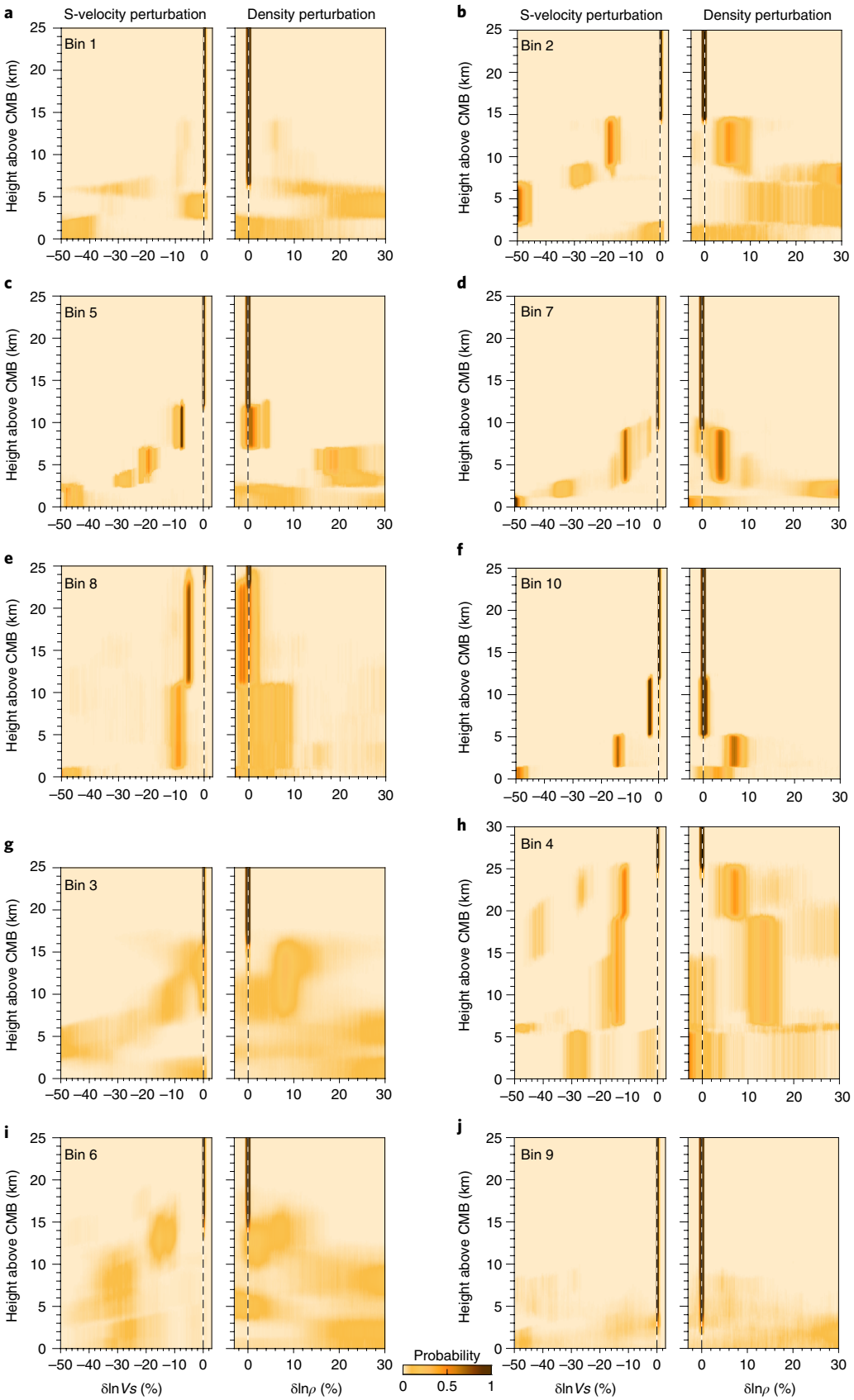

Fig. 2 | Inversion results in terms of S-wave velocity and density. a–j, S velocity (left) and density (right) as a function of depth for ten geographical bins. The results in **a–f** and **g–j** represent well- and weakly constrained ULVZs, respectively. Dark colours represent high probability density with the scale clipped at unity. Prior bounds for ULVZ parameters correspond to the plot widths.

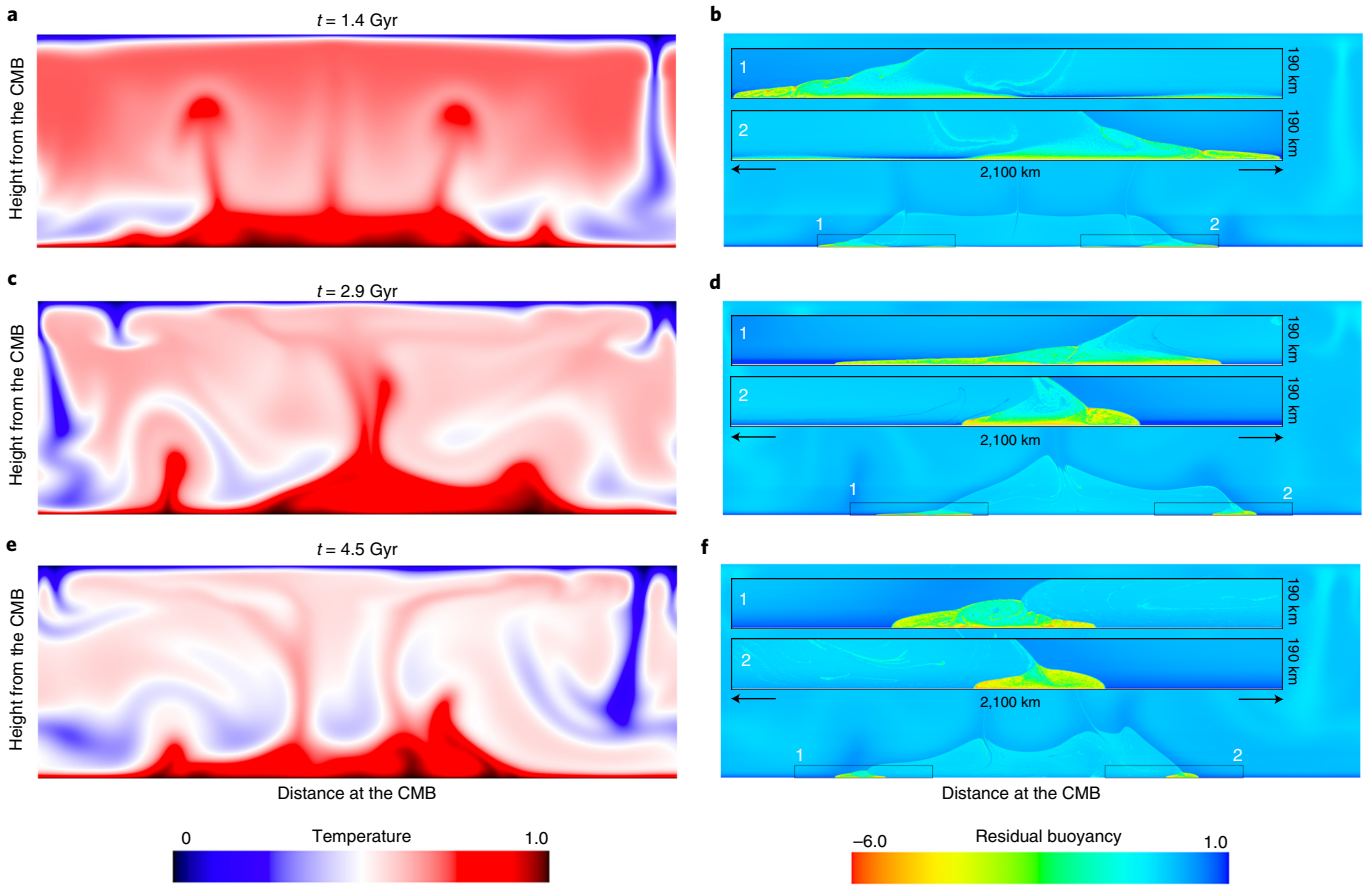

Fig. 3 | High-resolution geodynamic modelling results. a–f, Snapshots of the temperature field (**a**,**c**,**e**) and the residual buoyancy field (**b**,**d**,**f**) for the geodynamic model (case 1). In the residual buoyancy panels, the inset figures are zoomed in from the locations marked by numbers near the bottom of the model domain.

computer simulations in which data were simulated for various ULVZ geometries given by 2D Gaussian and boxcar shapes with one and three layers (Supplementary Fig. 2 and Supplementary Table 2). Subsequently, the simulated data were analysed with a 1D forward model. The results for these simulations illustrate that, when we take into account the trade-off between ULVZ properties, 1D inversions can still retrieve ULVZ properties within uncertainty as long as the ScP hits more than one degree away from the ULVZ edge. If ULVZs have a sharp boundary (boxcar case), ScP multi-pathing occurs when the bounce point is near the ULVZ boundary. In this case, the retrieved ULVZ parameters are poorly constrained and have larger uncertainties (Supplementary Information and Supplementary Figs. 3–15). We note that the Bayesian inversion also quantifies the trade-off between the ULVZ parameters. Trade-offs between parameter pairs can be visualized by joint marginal distributions (Supplementary Fig. 16), which indicate that there is a strong trade-off between S-velocity perturbation and thickness, as both parameters are constrained by the position and amplitude of the postcursors. Similarly, there is a strong trade-off between density and P-velocity perturbation, because these parameters are constrained by precursor amplitudes.

The results are for a southwest to northeast transect spanning a lateral distance of ~800 km along the CMB. The earthquake locations allow partitioning of the transect into ten geographic bins (Fig. 1c) and the interpretation of spatial variability. The bins are defined based on earthquake locations and are numbered from high-velocity (southwest) to low-velocity (northeast) zones in the lowermost mantle. Figure 2 shows our results in terms of the probabilities of S-wave velocity and density, and Extended Data Figs. 3–7 show the results in terms of interface depth, P-wave velocity, S-wave velocity and density for all bins. Extended Data Figs. 3–7 also show the observed data used in the inversion and the data predictions for a large ensemble of inferred parameters to illustrate their predictive ability. The results reveal two structural types of ULVZ. The first type exhibits a multi-layered, well-constrained ULVZ (bins 1, 2, 5, 7, 8 and 10 in Fig. 2a–f; Extended Data Figs. 3–5) and the second class a multi-layered, weakly constrained ULVZ (bins 3, 4, 6 and 9 in Fig. 2g–j; Extended Data Figs. 6 and 7). For well-constrained solutions, we make three key observations: the data support a multi-layered ULVZ in which (1) S-wave velocity decreases with depth, (2) density increases with depth and (3) ULVZs are thicker at the LLSVP edges and thinner within and outside the LLSVPs.

At bin 1, located in the high-velocity region of the S-velocity model, the ULVZ is thin, with a height of ~3 km and an ~38–50% S-wave velocity decrease (Fig. 2a and Extended Data Fig. 3). As we move to low S-velocity regions, the ULVZ height increases to ~15 km with S-wave velocity decreases up to 50% and density increases up to 30% as a function of depth (bin 2 in Fig. 2b; Extended Data Fig. 3). Similar reductions of S-wave velocity exist for bins 5, 7 and 10, but with decreased heights towards the centre of the LLSVP (Fig. 2c–e and Extended Data Figs. 4 and 5). Near the LLSVP edge, the ULVZ height is at a maximum (~23.0 km), with weaker S-wave velocity perturbations (bin 8 in Fig. 2e; Extended Data Fig. 5). Bin 3 is located ~65 km from bin 2 and its results (Fig. 2g and Extended Data Fig. 6) are similar to those for bin 2 but

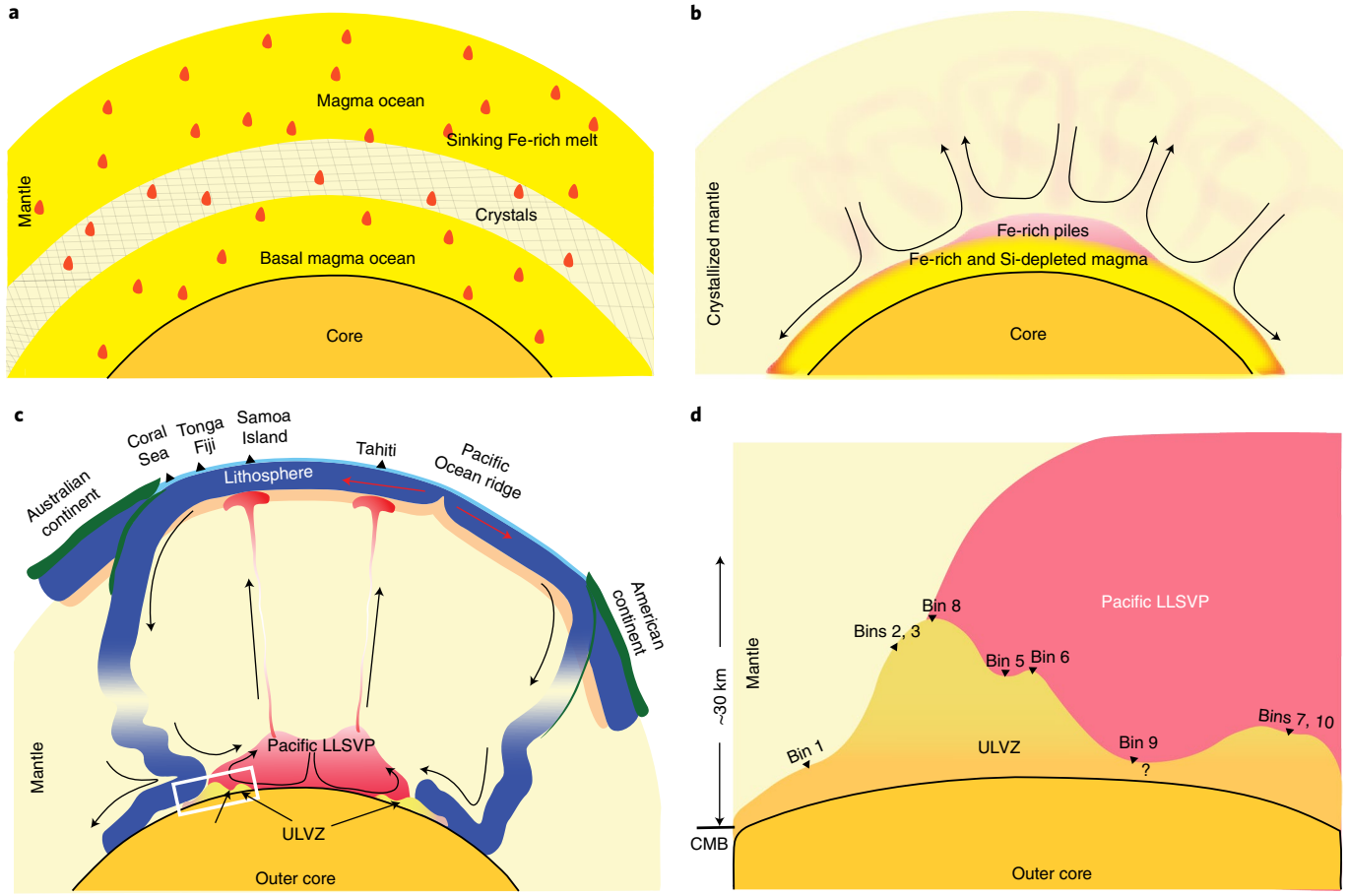

Fig. 4 | Schematic representation of the ULVZ, its evolution and the dynamic processes in the mantle. a, The sinking, due to gravity, of dense iron-rich melt through crystals formed as a result of cooling. **b**, Crystal growth in the mantle. For simplicity, crystal shapes are removed and represented only by colour. **c**, The ULVZs observed in this study, as well as other heterogeneities and dynamic processes in the mantle. Note that the vertical extent of the ULVZs and LLSVP is exaggerated for visualization purposes. **d**, Morphological representation of the ULVZs detected in this study. The numbers indicate the sampling bins at the CMB that are shown in Fig. 1c. The symbol '?' indicates a highly uncertain ULVZ. Colour variation within the ULVZ represents a stronger decrease in velocity and increase in density as a function of depth.

with larger uncertainties due to a lack of data (only 12 waveforms are available; Extended Data Fig. 1c). This similarity is evidence that the results do not depend on the earthquake characteristics. In contrast, bin 4 is located adjacent to bin 5, but its results differ substantially (Fig. 2h and Extended Data Fig. 6) due to the P-waveform complexity (Extended Data Fig. 2; see the Methods for details). The inversion results for bin 9 indicate a thin ULVZ with large uncertainties, although this bin has numerous waveforms with point-like sampling at the CMB (Fig. 1c). The interface probability shows a poorly estimated interface with probability between 0- to 9-km height (Fig. 2j and Extended Data Fig. 7).

Origin and dynamics of internally heterogeneous ULVZs

To study the dynamical implications of our results, we carried out very-high-resolution geodynamic models (1-km resolution in the lowermost 100 km of the mantle) and found that the ULVZ morphology discovered here can be explained by the presence of compositional heterogeneities within the ULVZ. For technical details on the geodynamic modelling, see the Methods. We initially introduce a global layer of LLSVP materials from 40 to 200 km above the CMB with intrinsic (that is, compositional) density 1.5% greater than the background mantle. In addition, a global layer of ULVZ materials is introduced in the lowermost 40 km of the mantle. In case 1, the density in the ULVZ layer increases exponentially from 1.5% intrinsically denser at 40 km above the CMB to 15.0% intrinsically denser at the CMB. After the initial condition, the global layer of LLSVP materials is pushed into a thermochemical pile by mantle flow, and the ULVZ materials gradually move to the edges of the thermochemical pile.

Figure 3 shows a time series of snapshots for the temperature field (Fig. 3a,c,e) and the residual buoyancy field (for example, the buoyancy field with the horizontal average removed; Fig. 3b,d,f). The ULVZ patches at the edges of the thermochemical pile have triangular shapes, and they are thicker in the middle and thinner at both flanks (Fig. 3b,d,f and Supplementary Video 1). In the middle of the ULVZ patches, the magnitude of the negative residual buoyancy increases with depth, while the residual buoyancy becomes more homogeneous towards the margins of the ULVZ patches (Fig. 3b,d,f). The increase of the density anomaly (or the magnitude of negative residual buoyancy) of the ULVZ patches with depth is more prominent during the early stages of the calculation (for example, Fig. 3b,d), and this phenomenon gradually becomes weaker due to mixing. However, the density anomaly of ULVZs is still increasing with depth after 4.5 Gyr (Fig. 3f). Notably, the features of ULVZ patches in this geodynamic model are consistent with the observed ULVZs where density increases with depth and thickness decreases farther into the LLSVPs. The distinct composition of the ULVZs and the increase of density and temperature as a function of ULVZ depth may explain the decrease of S-wave velocity with depth. Considering that the ULVZ patches are

compositionally heterogeneous, the different depth gradient of the P-wave velocity in bins 5 and 10 and the anticorrelation between P- and S-wave velocity anomalies in bin 10 can be seen in Fig. 3b,d,f. In addition, high-resolution geodynamic modelling supports that the seismologically observed internal discontinuities within the ULVZ are caused by incomplete mixing (Fig. 3b,d,f). Our modelling also explains the spatial variations of density and velocity within the ULVZs as well as a rapid spatial change of ULVZ thickness (Fig. 4).

We find that the spatial variability within the ULVZ patches homogenizes faster when the initial density contrast of the ULVZ layer and/or the viscosities of the ULVZ materials are reduced. For example, by reducing the range of the initial density anomaly of the ULVZ layer to 1.5–10% (case 2) or by reducing the intrinsic ULVZ viscosity by 100 times (case 3), the density variations within the ULVZ patches in both cases are much smaller than in case 1 after the same model time (Extended Data Fig. 8). The mixing rate within the ULVZ may also be controlled by factors such as the vigour of mantle convection, the temperature dependence of the viscosity and the density and viscosity of the LLSVPs. Nevertheless, our geodynamic modelling experiments demonstrate that, to survive viscous mixing, at least until present day, the initial density variations within the ULVZs need to be sufficiently large (that is, similar or higher than those in case 1). Here, we interpret the ULVZs as remnants of the crystallization of basal magma ocean, as a gradual crystallization of basal magma ocean that may lead to an initially global layer of dense materials whose density increases with depth[27]. However, intrinsically dense compositional heterogeneities can be continuously introduced to the CMB by subduction[27,28] and the core–mantle interaction[29], and future work needs to test whether and how these mechanisms could introduce materials with substantial density variations to the lowermost mantle.

The interpretation of the seismic observations with geodynamic modelling is summarized in Fig. 4. In the initial molten stage of the magma ocean, dense materials sink downwards due to gravitational instabilities[15]. The magma ocean starts to crystallize from the middle (Fig. 4a) and crystallizes faster towards the surface and slower towards the CMB as a result of the different heat fluxes near the surface and the CMB (Fig. 4b). As the magma ocean crystallizes, the light silicon depletes from the deep mantle and the melt becomes increasingly iron-enriched, which in turn increases the intrinsic density[30,31]. As a result, a layer of intrinsically dense materials remains after the crystallization of the basal magma ocean, and the intrinsic density of this layer increases with depth[29] (Fig. 4b). The global layer of intrinsically dense ULVZ materials on the CMB is later pushed by mantle flow into isolated ULVZ patches with variable and substantial topography near the edges of the LLSVPs (Fig. 4c,d), and the depth dependence of the intrinsic density anomaly of the ULVZs persists until the present.

Online content

Any methods, additional references, Nature Research reporting summaries, source data, extended data, supplementary information, acknowledgements, peer review information; details of author contributions and competing interests; and statements of data and code availability are available at https://doi.org/10.1038/s41561-021-00871-5.

Received: 6 November 2019; Accepted: 10 November 2021;
Published online: 30 December 2021

References

1. Li, X. D. & Romanowicz, B. Global mantle shear-velocity model developed using nonlinear asymptotic coupling theory. *J. Geophys. Res.* **101**, 22245–22272 (1996).
2. Ritsema, J., Deuss, A., van Heijst, H. J. & Woodhouse, J. H. S40RTS: a degree-40 shear-velocity model for the mantle from new Rayleigh wave dispersion, teleseismic traveltime and normal-mode splitting function measurements. *Geophys. J. Int.* **184**, 1223–1236 (2011).
3. Yu, S. & Garnero, E. J. Ultralow velocity zone locations: a global assessment. *Geochem. Geophys. Geosyst.* **19**, 396–414 (2018).
4. Garnero, E. J. & Helmberger, D. A very slow basal layer underlying large-scale low velocity anomalies in the lower mantle beneath the Pacific: evidence from core phases. *Geophys. J. Int.* **178**, 503–512 (1995).
5. Garnero, E. J. & Helmberger, D. Seismic detection of a thin laterally varying boundary layer at the base of the mantle beneath the central-Pacific. *Geophys. Res. Lett.* **23**, 977–980 (1996).
6. Thorne, M. & Garnero, E. J. Inferences on ultralow-velocity zone structure from a global analysis of SPdKS waves. *J. Geophys. Res.* **109**, B08301 (2004).
7. Williams, Q. & Garnero, E. J. Seismic evidence for partial melt at the base of Earth's mantle. *Science* **273**, 1528–1530 (1996).
8. Revenaugh, J. & Meyer, R. Seismic evidence of partial melt within a possibly ubiquitous low-velocity layer at the base of the mantle. *Science* **277**, 670–674 (1997).
9. Williams, Q., Revenaugh, J. & Garnero, E. J. A correlation between ultra-low basal velocities in the mantle and hot spots. *Science* **281**, 546–549 (1998).
10. Yuan, K. & Romanowicz, B. Seismic evidence for partial melting at the root of major hot spot plumes. *Science* **357**, 393–397 (2017).
11. Ross, A., Thybo, H. & Solidilov, L. Reflection seismic profiles of the core-mantle boundary. *J. Geophys. Res.* **109**, B08303 (2004).
12. Thorne, M. S., Takeuchi, N. & Shiomi, K. Melting at the edge of a slab in the deepest mantle. *Geophys. Res. Lett.* **46**, 8000–8008 (2019).
13. Idehara, K. Structural heterogeneity of an ultra-low velocity zones beneath the Philippine Islands: implications for core-mantle chemical interactions induced by massive partial melting at the bottom of the mantle. *Phys. Earth Planet. Inter.* **184**, 80–90 (2011).
14. Brown, S. P., Thorne, M. S., Miyagi, L. & Rost, S. Compositional origins to ultralow-velocity zones. *Geophys. Res. Lett.* **42**, 1039–1045 (2015).
15. McNamara, A. K., Garnero, E. J. & Rost, S. Tracking deep mantle reservoirs with ultra-low velocity zones. *Earth Planet. Sci. Lett.* **299**, 1–9 (2010).
16. Li, M., McNamara, A. K., Garnero, E. J. & Yu, S. Compositionally-distinct ultra-low velocity zones on Earth's core–mantle boundary. *Nat. Commun.* **8**, 177 (2017).
17. Labrosse, S., Hernlund, J. W. & Coltice, N. A crystallizing dense magma ocean at the base of the Earth's mantle. *Nature* **450**, 866–869 (2007).
18. Buffett, B. A., Garnero, E. J. & Jeanloz, R. Sediments at the top of Earth's core. *Science* **290**, 1338–1342 (2000).
19. O'Rourke, J. G. & Stevenson, D. J. Powering Earth's dynamo with magnesium precipitation from the core. *Nature* **529**, 387–389 (2016).
20. Christensen, U. R. & Hofmann, A. W. Segregation of subducted oceanic crust in the convecting mantle. *J. Geophys. Res.* **99**, 19867–19884 (1994).
21. Dobson, D. P. & Brodholt, J. P. Subducted banded iron formations as a source of ultralow-velocity zones at the core–mantle boundary. *Nature* **434**, 371–374 (2005).
22. Rost, S., Garnero, E. J., Williams, Q. & Manga, M. Seismological constraints on a possible plume root at the core–mantle boundary. *Nature* **435**, 666–669 (2005).
23. Rost, S. & Revenaugh, J. Seismic detection of rigid zones at the top of the core. *Science* **294**, 1911–1914 (2001).
24. Pachhai, S., Tkalčić, H. & Dettmer, J. Bayesian inference for ultralow velocity zones in the Earth's lowermost mantle: complex ULVZ beneath the east of Philippines. *J. Geophys. Res.* **119**, 8346–8365 (2014).
25. Pachhai, S., Dettmer, J. & Tkalčić, H. Ultra-low velocity zones beneath the Philippine and Tasman Seas revealed by a trans-dimensional Bayesian waveform inversion. *Geophys. J. Int.* **203**, 1302–1318 (2015).
26. Chapman, C. H. & Orcutt, J. A. The computation of body wave seismogram in laterally homogeneous media. *Rev. Geophys.* **23**, 105–163 (1985).
27. Ballmer, M. D., Lourenco, D. L., Hirose, K., Caracas, R. & Nomura, R. Reconciling magma–ocean crystallization models with the present-day structure of the Earth's mantle. *Geochem. Geophys. Geosyst.* **18**, 2785–2806 (2017).
28. Li, M., McNamara, A. K. & Garnero, E. J. Chemical complexity of hotspots caused by cycling oceanic crust through mantle reservoirs. *Nat. Geosci.* **7**, 366–370 (2014).
29. Kanda, R. V. S. & Stevenson, D. J. Suction mechanism for iron entrainment into the lower mantle. *Geophys. Res. Lett.* **33**, L02310 (2006).
30. Solomatov, V. S. & Stevenson, D. J. Nonfractional crystallization of a terrestrial magma ocean. *J. Geophys. Res. Atmos.* **98**, 5391–5406 (1993).
31. Abe, Y. Thermal and chemical evolution of the terrestrial magma ocean. *Phys. Earth Planet. Int.* **100**, 27–39 (1997).

Methods

Data processing. This study utilizes the waveforms of the Earth's core-reflected waves (ScP) recorded on the vertical-component seismograms of seismic arrays operated by the Research School of Earth Sciences at the Australian National University. We consider data from three temporary arrays, the WOMBAT and SQspa arrays in Queensland and Tasmania and the Warramunga array (WRA) in the Northern Territory. The instrument spacing for WOMBAT is ~50 km in Queensland and ~20 km in Tasmania, whereas the station spacing for the SQspa array is 3–4 km. The WRA in the Northern Territory consists of a small-aperture array with broadband seismometers, with two arms intersecting in a letter-L shape of 20 elements spaced ~2 km apart, supplemented by an additional four sites near the intersection. Projected onto the CMB, this configuration of stations corresponds to maximum separations of ~1.5 km, ~7.0 km and ~25.0 km between ScP piercing points at the CMB for the SQspa, WRA and WOMBAT arrays, respectively. There are 24 stations for the WRA array, 27 for the WOMBAT array and 36 for SQspa. The waveforms from individual stations were visually inspected, and those with glitches and low signal-to-noise ratio were discarded.

We considered earthquakes originating in Tonga, Fiji and Vanuatu from the southwest Pacific subduction zones from 2001 to 2014. The events had to satisfy the following criteria: (1) vertical component seismograms with good signal-to-noise ratio, (2) hypocentre depth of >80 km to avoid contamination by depth phases, (3) magnitude between 5.0 and 6.5 for which the source-time functions are relatively simple and (4) an epicentral distance greater than 20°. Any PcP and ScP phases that were contaminated by direct S waves were eliminated. We also performed array analysis of the recorded waveforms over the array and found no mixing with other phases. The use of deep-focus earthquakes and vertical component recordings reduces the possibility of interference between ScP and PcS waves. We also discarded events that were suspected to be contaminated by shallow structures or source complexities. Of the 1,282 events that were examined, 72 satisfied the criteria, with clear onsets of ScP phases. However, there were not many events that showed simultaneous and clear onsets of P, PcP or ScP arrivals. In most events, onsets of ScP are clearer than PcP due to the higher reflection coefficients at the epicentral distance considered here. From the 72 selected events, we found 10 appropriate events with which to compute an empirical source-time function by the stacking of P waveforms. The source–receiver ray path and the source mechanism of the selected events are shown in Fig. 1b,c and the hypocentral parameters are presented in Supplementary Table 1. The source information shows a similar earthquake mechanism for the events.

We applied a wide range of high-pass filters, band-pass filters and combinations of the two with various corner frequencies to visually inspect the onsets of the P, PcP and ScP phases. Band-pass filters with 0.5-Hz and 1.5-Hz corners produced the clearest onsets. We then applied iterative adaptive stacking[32] to compute the empirical source-time, which includes source, near-receiver and path effects. We previously deconvolved stacked PcP waveforms from ScP waveforms[24,25], as they share similar paths in the upper mantle. However, the simultaneous observation of PcP and ScP waves is more challenging than for P and ScP waves. In addition, PcP waveforms can be contaminated by ULVZ features. We thus deconvolved a stack of P waveforms to remove the source and near-receiver effects. We found that deconvolution of the P or PcP wavelet from the ScP waveforms gave similar results, with 95% cross-correlation coefficient if the source was simple and the PcP did not sample the ULVZ. As the deconvolved ScP waveforms are similar, the inversion for these two waveforms results in two-layer ULVZ models. The top layer has a height of ~7 km with an approximately 5% decrease in S velocity, whereas the bottom layer has a height of ~3 km with an approximately 45% decrease in S velocity. Note that the P and ScP waveforms have different source radiation patterns. However, amplitude normalization and deconvolution of P from the ScP waveforms mitigate the effect of the source radiation pattern. Additionally, there is no polarity reversal between P and ScP, as both phases leave the same quadrant, although their take-off angles are different (Fig. 1c). The deconvolved ScP waveforms from the selected events are shown in Extended Data Fig. 1.

Trans-dimensional Bayesian inversion. This Article employs a hierarchical trans-dimensional (trans-D) Bayesian inversion to quantify 1D ULVZ parameter values and their uncertainties[25]. In this approach, the numbers of ULVZ layers and noise parameters (a parameterized noise covariance matrix including off-diagonal terms) are treated as unknown to avoid subjective assumptions[33]. The solution to the inverse problem is the PPD, which is obtained by updating prior information with the data information given by the likelihood function. For a vector of N measured data, $\mathbf{d}$, Bayes' theorem for a trans-D model can be expressed as[34]

$$p\,(k, \mathbf{m}_k\,|\mathbf{d}\,) \propto p(k)p\,(\mathbf{d}\,|k, \mathbf{m}_k\,)\,p\,(\mathbf{m}_k\,|k\,), \quad (1)$$

where $\mathbf{m}_k$ is the model parameter vector of M parameters with k interfaces, $p(k)$ is the prior probability for the number of interfaces, $p(\mathbf{m}_k|k)$ is the prior for thickness, P velocity, S velocity and density for an elastic layer, and $p(k,\mathbf{m}_k|\mathbf{d})$ is the PPD. For observed data, $p(\mathbf{d}|k,\mathbf{m}_k)$ represents the likelihood of the model parameters, a function of the model parameters. The likelihood function is derived assuming Gaussian-distributed data errors. The data errors are typically unknown, but approximated by residual errors. For measured data, errors are often correlated, and such correlation is accounted for in the inversion using an autoregressive process of order 1 (AR1).

For nonlinear inverse problems such as waveform inversion, no analytical solution exists for the PPD, and we apply reversible jump Markov chain Monte Carlo (rjMCMC) sampling to compute the PPD. The rjMCMC generalizes the Metropolis–Hasting acceptance rule such that jumps between models with different parameter dimensions (from 0 to 4 interfaces) are allowed via birth and death moves[35]. For birth moves, a new interface is created at a random position between the CMB and the maximum height of interest, and a random interface is deleted in the case of a death move. Perturbation moves are applied to perturb layer parameters without changing the model dimension. These three types of move are accepted or rejected based on the Metropolis–Hasting acceptance criterion. If the model is kept, the parameter is updated and the process is repeated, whereas the parameter is retained if the model is rejected. More details are available in previous works[24,25].

Geodynamic modelling. We solved the conservation equations of mass, momentum and energy under the Boussinesq approximation using the 2D CITCOM code. The model contains three compositional components, including regular background mantle materials and two compositional components to simulate the LLSVPs and ULVZs, which are referred to as LLSVP materials and ULVZ materials, respectively. The intrinsic (compositional) density anomaly is represented by the non-dimensional buoyancy number, which is defined as the ratio between the intrinsic density anomaly and the density anomaly caused by thermal expansivity, or $B=\Delta\rho/(\rho_0\alpha_0\Delta T)$, where $\Delta\rho$ is the intrinsic density anomaly, ρ_0 is the reference density (we use the density of the background mantle material as reference), α_0 is the reference thermal expansivity and ΔT is the temperature difference between the CMB and the surface. In this study, we use $\rho_0=3{,}300\,\mathrm{kg\,m^{-3}}$, $\alpha_0=1\times10^{-5}\,\mathrm{K^{-1}}$ and $\Delta T=2{,}500\,\mathrm{K}$. The buoyancy, or the net dimensionless density anomaly ρ_{net}, for each element of the model domain is computed by summing the contributions from both thermal expansion and the intrinsic density anomaly and is given by $\rho_{\mathrm{net}}=T-B^{\mathrm{ave}}$, with T being the dimensionless temperature and B the average buoyancy ratio of the element.

Here, one of the goals of geodynamic modelling is to place constraints on the mechanism generating seismic heterogeneities within ULVZs. The existence of small-scale seismic heterogeneities within ULVZs requires chemical heterogeneities. We thus performed a numerical modelling experiment to demonstrate a mechanism to generate and maintain chemical heterogeneities within ULVZs. We found that whether there remain chemical heterogeneities within the present-day ULVZs strongly depends on the rate of chemical mixing. The difference in mixing rate between 2D and 3D models has been extensively studied before[36,37] and, through systematic geodynamic modelling experiments, it was found that 2D and 3D models have similar mixing rates. We therefore used 2D models because they allow higher model resolution than 3D models, which is essential in this study given the small size of ULVZs. The 2D model in Cartesian geometry has an aspect ratio of 3:1. There are 3,072 and 512 elements in the horizontal and vertical directions, respectively. The grid mesh is further refined in the lowermost 100 km of the model, resulting in a vertical resolution of 1 km at this depth range. We used the ratio tracer method[38] to simulate the advection of the compositional field, and 157 million tracers were used.

We used a Rayleigh number of $\mathrm{Ra}=10^7$ in the geodynamic model. The temperature-dependent viscosity was $\eta_T=\exp(A(0.5-T))$, with activation energy $A=6.91$. In addition, a 50 times viscosity increase was applied from the upper mantle to the lower mantle. The top and bottom boundaries were free-slip and isothermal, with $T=0$ and $T=1$ on the top and bottom boundaries, respectively. The side boundaries were periodic. The initial temperature was relatively high, with $T=0.72$ (or 1,800 K) everywhere, and includes small temperature perturbations, to simulate the early hot Earth's mantle.

We initially introduced a global layer of LLSVP materials from 40 km to 200 km above the CMB, with a buoyancy number of $B=0.6$, which makes it ~1.5% intrinsically denser than the background mantle. In addition, a global layer of ULVZ materials was introduced in the lowermost 40 km of the mantle, and its buoyancy number increased exponentially from $B=0.6$ (or 1.5% intrinsically denser) at 40 km above the CMB to $B=6.0$ (or 15% intrinsically denser) at the CMB in case 1 and $B=4.0$ (or 10% intrinsically denser) in case 2. Case 3 had the same parameters as case 1, except that the intrinsic viscosity of the ULVZ materials was reduced by 100 times.

Effect of complexities other than ULVZs. ScP waves are affected by various heterogeneities along their path, including seismic anisotropy. Of these heterogeneities, upper-mantle anisotropy is most substantial. Most ScP waveforms considered here are from earthquakes at depths of >500 km (Supplementary Table 1) and pre- and postcursors are observed for all events. This confirms that the upper-mantle anisotropy effects are minor. Previous studies found ~2.0% azimuthal anisotropy in the lowermost mantle[39–42]. However, the lowermost anisotropy alone cannot justify a decrease as large as 50% in the S velocity. Furthermore, although anisotropy from stacks of thin layers is feasible, such a structure would produce incoherent postcursors that would cancel during waveform stacking across stations. Finally, it is unlikely that the postcursors

are affected by vertically transverse isotropy, because the vertically polarized component arrives earlier than the ScP phase.

Similarly, attenuation along the ray path can also affect seismic observations. In this study we considered data from deep events to avoid source-side upper-mantle S-wave attenuation. Previous studies have indicated that the lowermost mantle, particularly LLSVPs, can be attenuative due to the hotter than average mantle[43]. If there is a strong attenuation along the ray path of the seismic waves, seismic attenuation can change both the amplitude and pulse width of the seismic phases (ScP wavelet in this case). In this study, we normalized the waveform by the ScP amplitude. Accordingly, there will be no effect on the inversion results from the change in ScP amplitude. However, broadening the ScP pulse width could impact the inversion results if there is a strong attenuation. To check to what extent attenuation in the deep mantle can affect our results, we computed a parameter that represents the attenuation along the ray path (t^*, which is reciprocal to the quality factor Q; that is, higher values of t^* indicate more substantial attenuation and vice versa). First we convolved a range of t^* values (from 0 to 1.0 in intervals of 0.1) with the P wavelet, which does not sample the deep mantle. We then compared the attenuated P wavelet with the associated ScP wavelet using L2-norm (Supplementary Fig. 1). This analysis showed that the minimum misfit (L2-norm) or the best agreement between P and ScP wavelets is achieved for the t^* value close to zero for all the events used in this study. In summary, our analysis indicates that there is no substantial effect of seismic attenuation in the inversion results.

In addition to seismic heterogeneity, it is also possible that various mechanisms (subducted slab, basal magma ocean and thermochemical or thermal pile) can produce positive and negative topography at the CMB. Various geodynamic modelling studies have examined the effect of CMB dynamic topography and attempted to link it with the possible origin of the LLSVPs[44,45], although this is still a matter of debate. Seismological studies also suggest long-wavelength CMB topography, up to spherical harmonic degree 4 (ref. [46]), and found a peak-to-peak amplitude on the order of a couple of kilometres. However, very-long-wavelength topography does not seem to affect the observational data we use, as the impedance contrast at the CMB does not change. It is possible that a small variation of the CMB depth can lead to substantial differences in the travel time of seismic phases that pass through such topography. However, any effect in the travel time of ScP does not impact our inversion results. This is because we align all the waveforms relative to the ScP arrival time. Accordingly, even if there is a strong long-wavelength topography at the CMB, our inversion results will not be altered.

More recently, other geodynamic studies have suggested CMB topography that is a few kilometres in amplitude and a shorter-length- scale topography (80–100 km)[47]. However, even with this length scale of topography, our observation would not carry such information, because sampling of the CMB due to a single event is within a few tens of kilometres. Furthermore, this short length scale will not affect the ScP waveforms unless the CMB topography has abrupt edges and the ScP bounce point happens to lie right along that boundary, as if we are internal to the topographic changes. However, we do not believe that strong boundary topographic effects are occurring here, because we do not see a wide variation of ScP precursors in our observations, even for such a worst-case scenario. Importantly, our observations show consistent precursors. Additionally, the employed inversion scheme must consistently fit the precursors and postcursors to constrain the ULVZ parameters. Moreover, the effect of the CMB topography is weaker than that resulting from the 2D/3D nature of the ULVZ, as presented in the Supplementary Information. Therefore, the impact of the CMB topography on the precursors is likely to be below the noise level, and the effect of topography cannot be more severe than some other approximations made in this study.

We have considered earthquakes with magnitude of less than 6.0 and discarded events with complex P waveforms. Therefore, it is unlikely that the inversion results are affected by source complexity. For example, we examined the inversion results for two events (bins 2 and 3) that sample slightly different locations within a one-quarter Fresnel zone (that is, 30 km). The inversion results are similar for these two locations, indicating that the structure is independent of the earthquakes used (Extended Data Figs. 3 and 6). By contrast, for two events (bins 4 and 5) that sample almost the same structure, the waveforms differ substantially (Extended Data Fig. 2). In particular, individual deconvolved waveforms show highly pronounced pre- and postcursor amplitudes in the case of bin 4 (Extended Data Fig. 2). To check whether waveform complexity comes from the earthquake source, we deconvolved the stacked P waveform after removing the signal that arrived ~2 s after the direct P wave that we suspect came from the source-side complexity. The stack of deconvolved waveforms shows a precursor with much smaller amplitude (Extended Data Fig. 2b), which indicates that the deconvolved waveform in the case of bin 4 is highly affected by the complexity in the P waveform. Therefore, the inversion results for this bin (presented in Fig. 2h and Extended Data Fig. 6) show a complexity that cannot be interpreted physically.

As for the receiver-side effects, we found little variability in the waveforms recorded by stations across the array. However, substantial waveform variability was observed for the various CMB sampling points. The incoherent variability cancels when stacking waveforms across stations. Moreover, we deconvolved an empirical source-time function derived from the stack of P waveforms that took into account the receiver-side and path effects. For example, bins 9 and 10 were recorded at WRA-array stations, but the stacked waveforms from these two events are different, although their magnitudes are similar and are recorded by the same stations. Similarly, if there is an effect of receiver-side complexity, the complexity must be observable for various events. We also note that the P and ScP waves have different source excitations, so the pulse width is considered by convolving a source-time function of observed P-wave pulse width. In contrast, previous studies considered the convolution of a P wavelet with synthetic ScP waveforms[48–50].

Data availability

All the data used in this study are freely available in the GitHub repository: https://github.com/pachhaisurya200/Pachhai_etal_2021_Data. Source data are provided with this paper.

Code availability

Bayesian inversion code is available from S.P. 2D forward computation code can be obtained from M.S.T. The 2D geodynamic modelling code CITCOM is publicly available[49,50].

References

32. Rawlinson, N. & Kennett, B. L. N. Rapid estimation of relative and absolute delay times across a network by adaptive stacking. *Geophys. J. Int.* **157**, 332–340 (2004).
33. Dettmer, J. & Dosso, S. E. Trans-dimensional matched-field geoacoustic inversion with hierarchical error models and interacting Markov chains. *J. Acoust. Soc. Am.* **132**, 2239–2250 (2012).
34. Green, P. J. Reversible jump Markov chain Monte Carlo computation and Bayesian model determination. *Biometrika* **82**, 711–732 (1995).
35. Geyer, C. J. & Moller, J. Simulation procedures and likelihood inference for spatial point processes. *Scand. J. Stat.* **21**, 359–373 (1994).
36. Coltice, N. & Schmalzl, J. Mixing times in the mantle of the early Earth derived from 2-D and 3-D numerical simulations of convection. *Geophys. Res. Lett.* https://doi.org/10.1029/2006gl027707 (2006).
37. O'Neill, C. J. & Zhang, S. Lateral mixing processes in the Hadean. *J. Geophys. Res. Solid Earth* **123**, 7074–7089 (2018).
38. Tackley, P. J. & King, S. D. Testing the tracer ratio method for modeling active compositional fields in mantle convection simulations. *Geochem. Geophys. Geosyst.* **4**, 8302 (2003).
39. Hall, S. A., Kendall, J.-M. & van der Baan, M. Some comments on the effects of lower-mantle anisotropy on SKS and SKKS phases. *Phys. Earth Planet. Int.* **146**, 469–481 (2004).
40. Garnero, E. J., Maupin, V., Lay, T. & Fouch, M. J. Variable azimuthal anisotropy in Earth's lowermost mantle. *Science* **306**, 259–261 (2004).
41. Wookey, J., Kendall, J.-M. & Rumpker, G. Lowermost mantle anisotropy beneath the north Pacific from differential S-ScS splitting. *Geophys. J. Int.* **161**, 829–838 (2005).
42. Nowacki, A., Wookey, J. & Kendall, J.-M. New advances in using seismic anisotropy, mineral physics and geodynamics to understand deformation in the lowermost mantle. *J. Geodyn.* **52**, 205–228 (2011).
43. Konishi, K., Fuji, N. & Deschamps, F. Elastic and anelastic structure of the lowermost mantle beneath the Western Pacific from waveform inversion. *Geophys. J. Int.* **208**, 1290–1304 (2017).
44. Lassak, T. M., McNamara, A. K., Garnero, E. J. & Zhong, S. Core–mantle boundary topography as a possible constraint on lower mantle chemistry and dynamics. *Earth Planet. Sci. Lett.* **289**, 232–241 (2010).
45. Deschamps, F., Rogister, Y. & Tackley, P. J. Constraints on core–mantle boundary topography from models of thermal and thermochemical convection. *Geophys. J. Int.* **212**, 164–188 (2018).
46. Tanaka, S. Constraints on the core-mantle boundary topography from P4KP-PcP differential travel times. *J. Geophys. Res.* **115**, B04310 (2010).
47. Heyn, B. H., Conard, C. P. & Tronnes, R. G. Core–mantle boundary topography and its relation to the viscosity structure of the lowermost mantle. *Earth Planet. Sci. Lett.* **543**, 116358 (2020).
48. Vidale, J. E. & Benz, H. A sharp and flat section of the core–mantle boundary. *Nature* **359**, 627–629 (1992).
49. Garnero, E. J. & Vidale, J. E. A probe of ultralow velocity zones at the base of the mantle. *J. Geophys. Res.* **26**, 277–380 (1999).
50. Castle, J. & der Hilst, V. The core–mantle boundary under the Gulf of Alaska: no ULVZ for shear waves. *Earth Planet. Sci. Lett.* **176**, 311–321 (2000).

Acknowledgements

We would like to acknowledge members of the Seismology and Mathematical Group of the Research School of Earth Sciences (RSES), The Australian National University (ANU), for maintaining the seismic networks considered in this study. We would also like to acknowledge the University of Utah Center for High Performance Computing, the Argo cluster at ICTP, and ANU Terrawulf cluster at RSES for computing resources. S.P. would like to acknowledge partial support from an ANU PhD scholarship and NSF

grant no. EAR-1723081. M.S.T. acknowledges partial support from NSF grant no. EAR-1723081. M.L. was supported by NSF grants nos. EAR-1849949 and EAR-1855624. The funders had no role in study design, data collection and analysis, decision to publish or preparation of the manuscript.

Author contributions

S.P. conceived this study during his PhD under the supervision of H.T. and J.D., performed all the data processing, analysis, waveform inversions and figures preparation, and wrote the first version of the manuscript. M.L. performed the geodynamical computation, prepared Fig. 3, Extended Data Fig. 8 and Supplementary Videos 1–3, and wrote the geodynamical method part. All authors discussed the results and shaped the manuscript to its final stage. M.S.T. and S.P. designed the 2D models. M.S.T. implemented the finite-difference PSVaxi code to compute the synthetic ScP waveforms for various 2D geometries.

Competing interests

The authors declare no competing interests.

Additional information

Extended data is available for this paper at https://doi.org/10.1038/s41561-021-00871-5.

Supplementary information The online version contains supplementary material available at https://doi.org/10.1038/s41561-021-00871-5.

Correspondence and requests for materials should be addressed to Surya Pachhai.

Peer review information *Nature Geoscience* thanks the anonymous reviewers for their contribution to the peer review of this work.Primary Handling editors: Simon Harold, Stefan Lachowycz

Reprints and permissions information is available at www.nature.com/reprints.

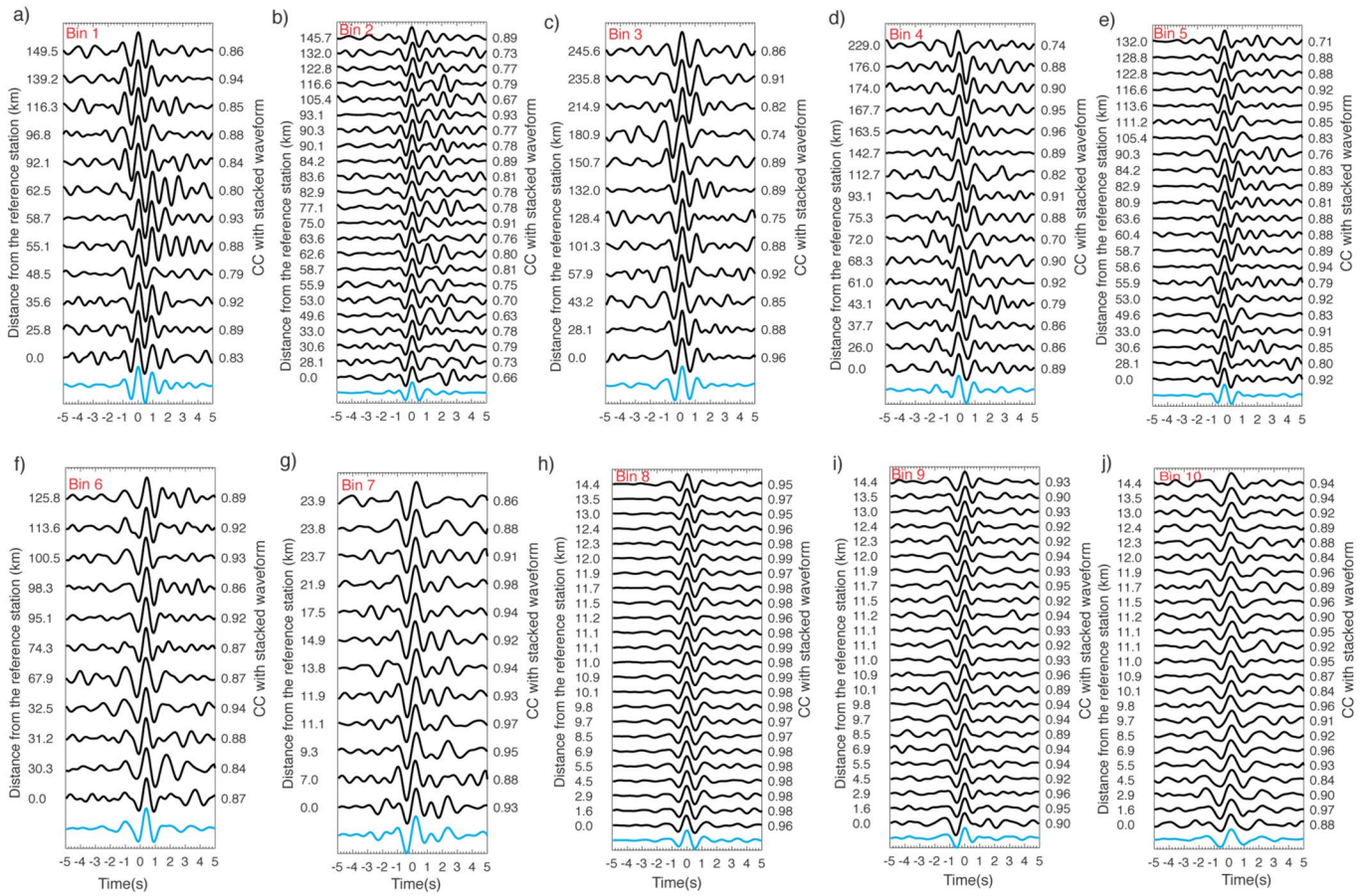

Extended Data Fig. 1 | Observed ScP waveforms. Individual ScP waveforms, after removing the source and path effects, sorted as a function of distance from the center of their respective geographical bins. Cross-correlation coefficients between stacked waveform (cyan color on the bottom panels) and individual waveforms are also shown.

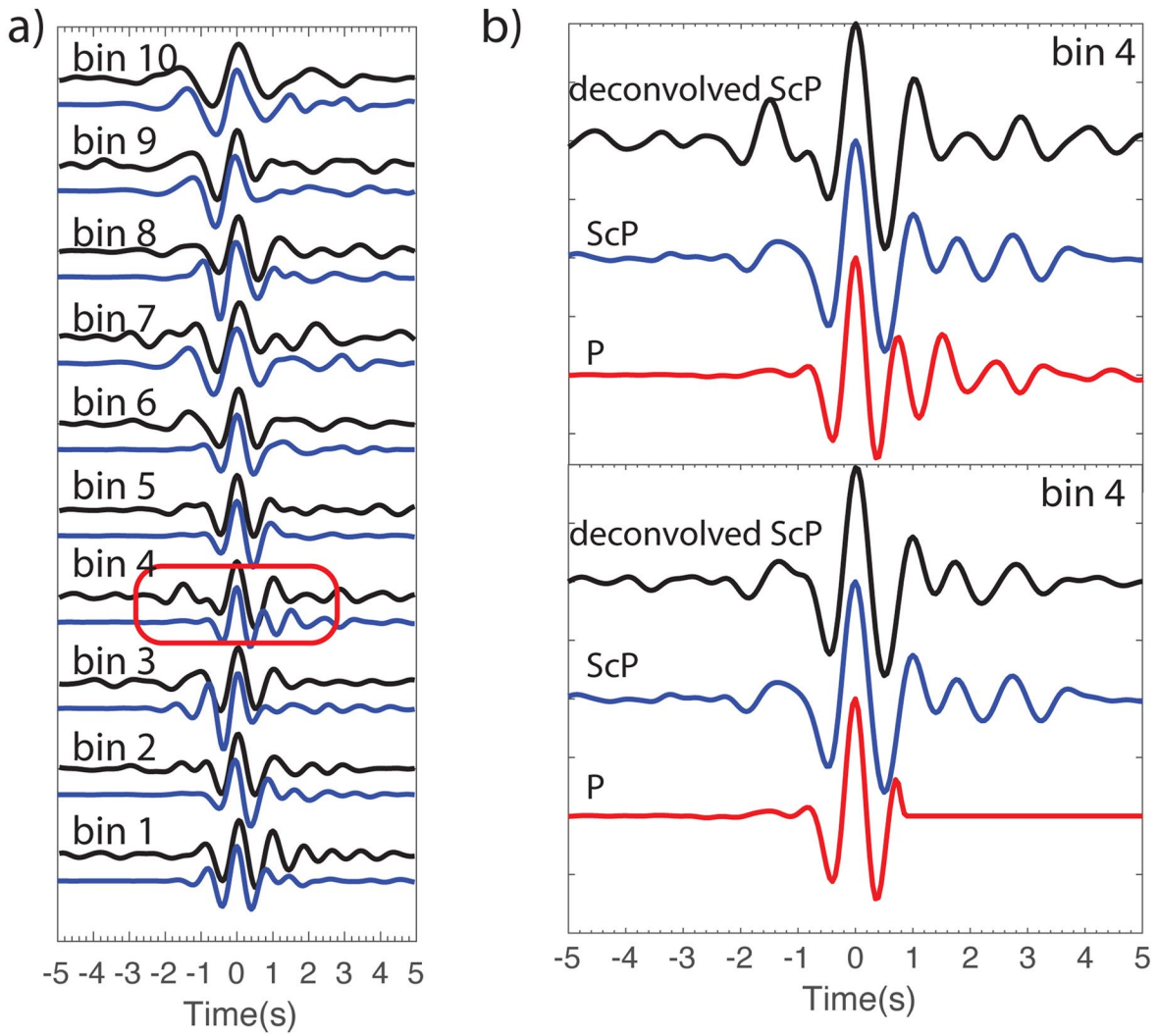

Extended Data Fig. 2 | Stacked ScP-waveforms. (**a**) Stack of deconvolved ScP-waveforms (black lines) with stacked P-waveforms (blue line) for different geographical bins analyzed in this study. (**b**) Example waveforms resulting from the effect of earthquake source complexity.

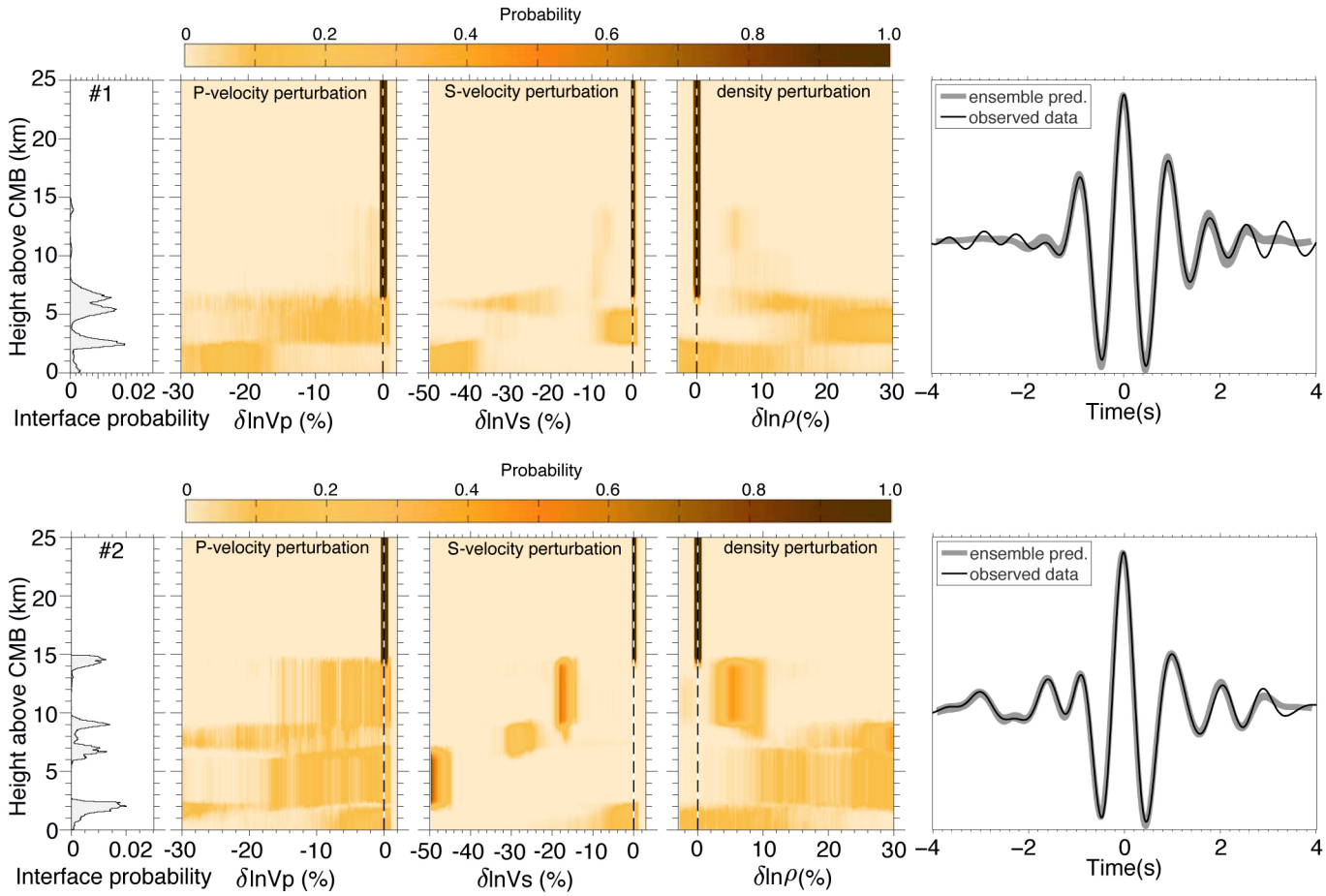

Extended Data Fig. 3 | Inversion results for bins 1 and 2. Posterior probability density of interfaces, and P-wave velocity, S-wave velocity and density as a function of depth, and observed and ensemble model predictions in the case of bin (top) 1 and (bottom) 2. The color represents the probability density with each depth interval normalized to unit probability. Dark color represents high probability density with the scale clipped at unity.

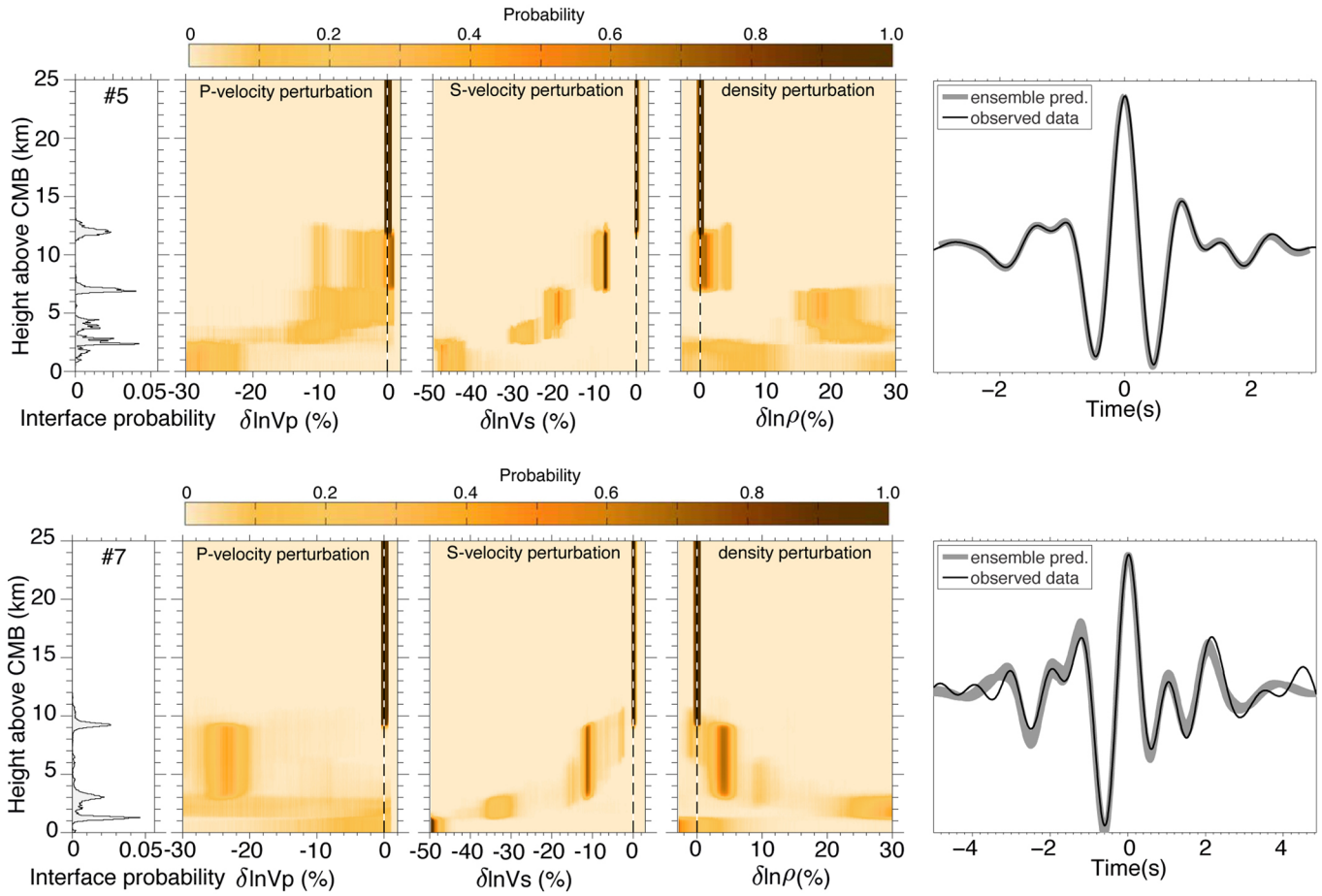

Extended Data Fig. 4 | Inversion results for bins 5 and 7. Same as Extended Data Fig. 3 but in the case of bins 5 (top) and 7 (bottom).

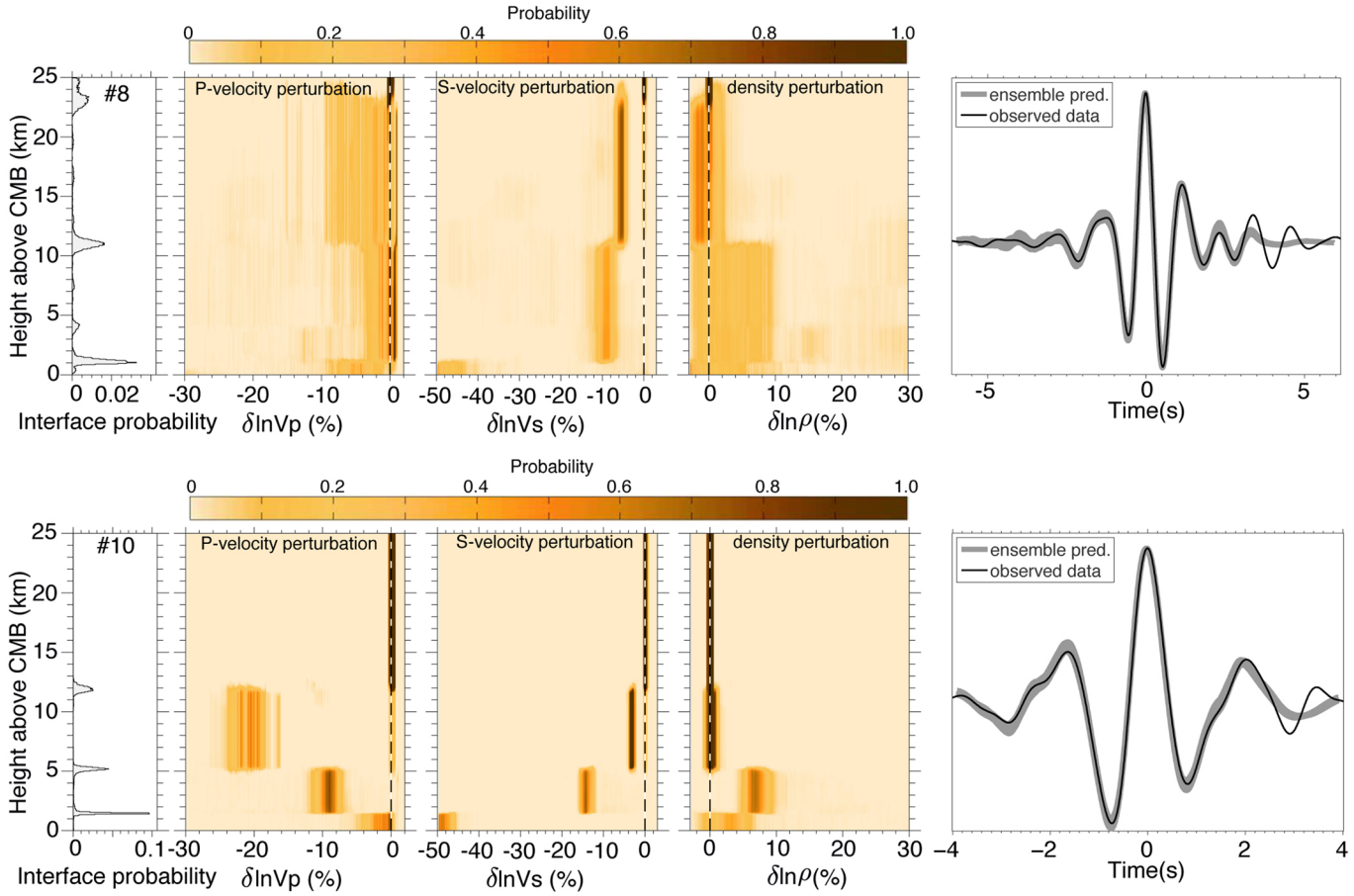

Extended Data Fig. 5 | Inversion results for bins 8 and 10. Same as Extended Data Fig. 3 but in the case of bins 8 (top) and 10 (bottom).

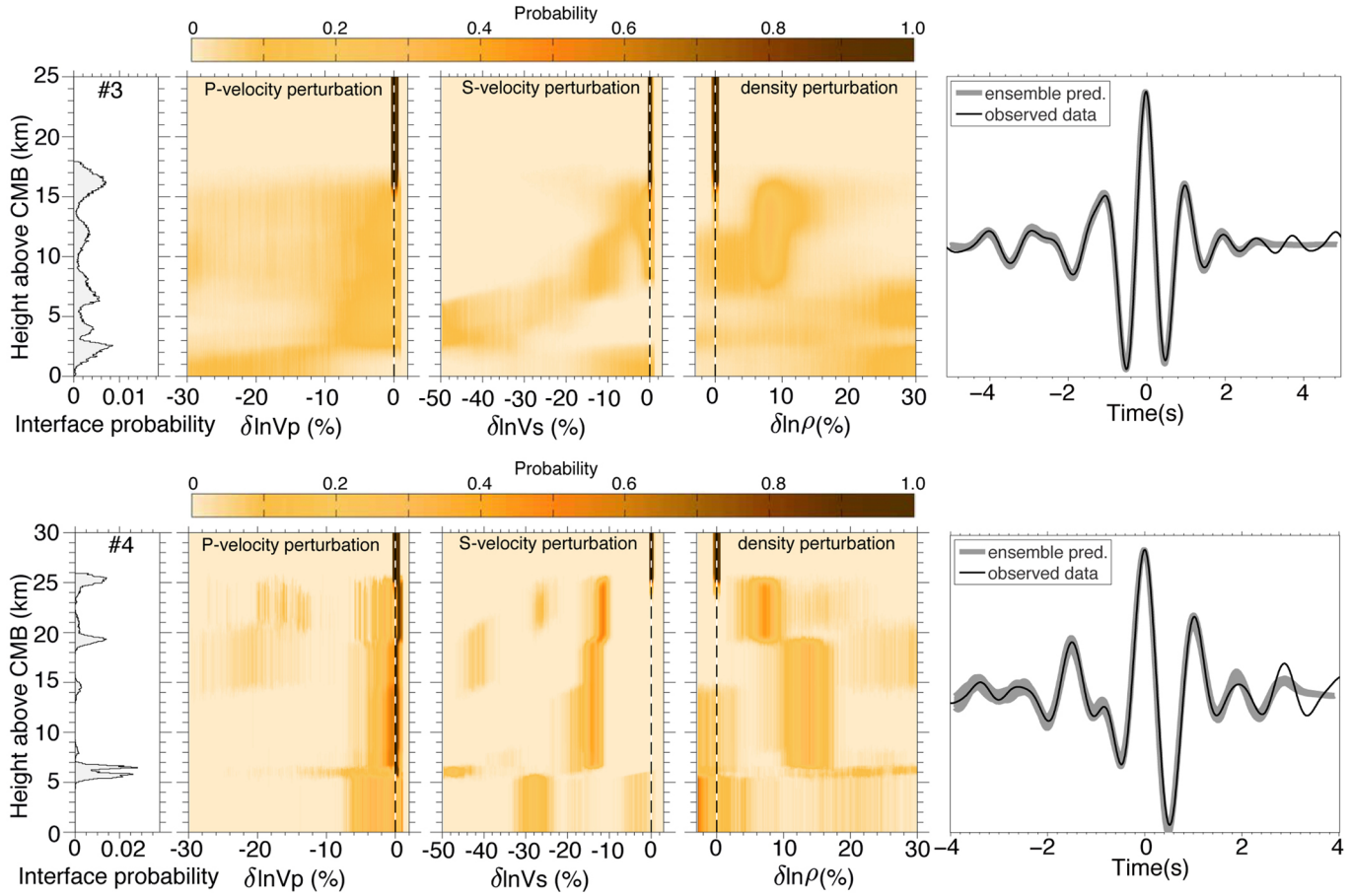

Extended Data Fig. 6 | Inversion results for bins 3 and 4. Same as Extended Data Fig. 3 but in the case of bin 3 (top) and 4 (bottom).

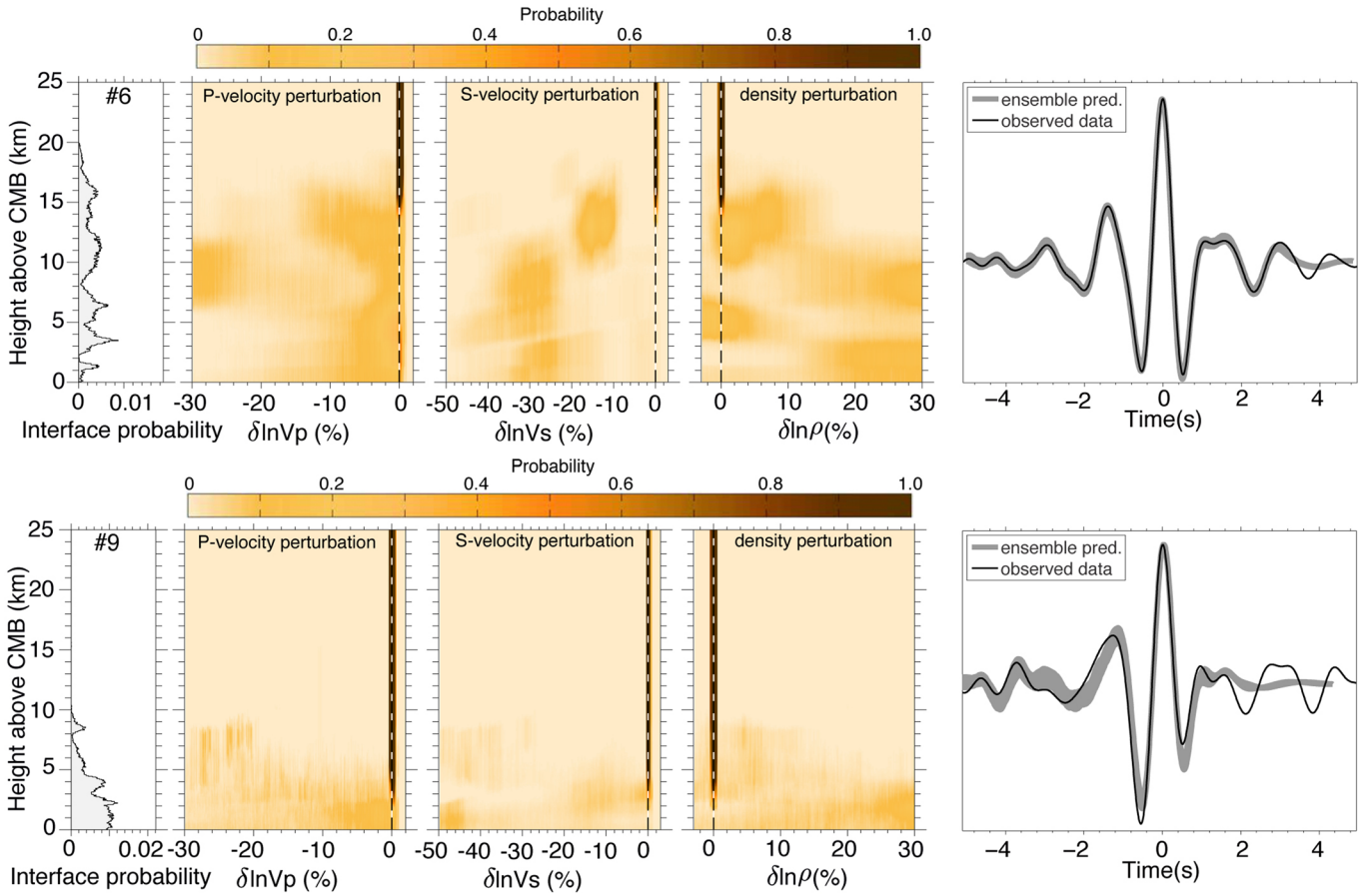

Extended Data Fig. 7 | Inversion results for bins 6 and 9. Same as Extended Data Fig. 3 but in the case of bin 6 (top) and 9 (bottom).

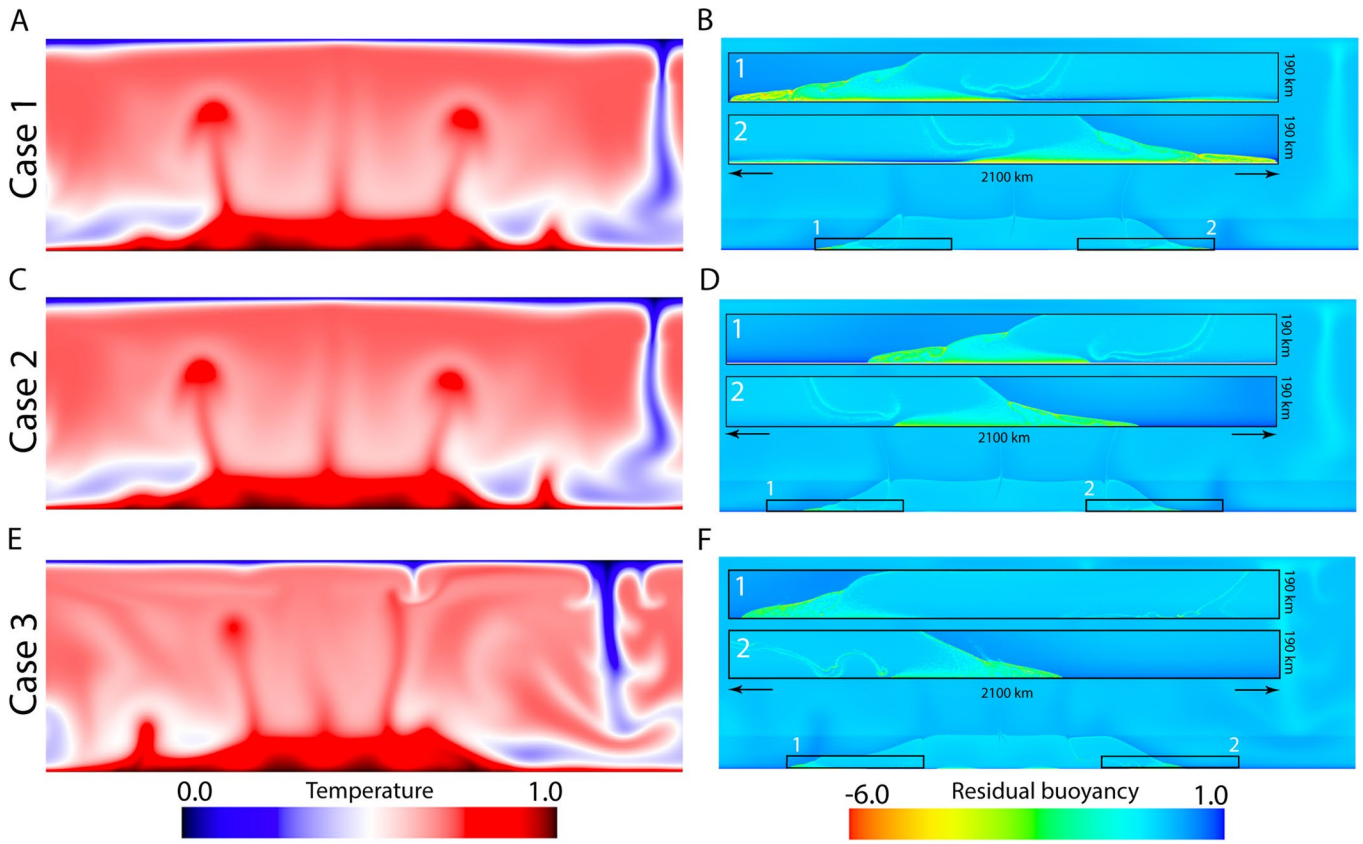

Extended Data Fig. 8 | High-resolution geodynamic modeling results. Snapshots of the temperature field (left column) and the residual buoyancy field (right column) for the case 1 (**A, B**), case 2 (**C, D**) and case 3 (**E, F**) after 1.4 Gyr. Case 1 is the reference case in which the initial density anomaly of the ULVZ layer ranges from 1.5 to 15%. Case 2 is the same as Case 1, expect that the initial density anomaly of the ULVZ layer ranges from 1.5 to 10%. Case 3 is the same as case 1 except that the ULVZ materials are intrinsically 100 times less viscous than the surrounding mantle. In the residual buoyancy panels, the inserted figures are zoomed in from the locations marked by the black box near the bottom of the model domain. Note that the density anomalies (represented by the residual buoyancy) with the ULVZ patches (zoomed in by the rectangle boxes) are more homogenized in case 2 (D) and case 3 (F) than in case 1 (B), whereas the large-scale structure are more similar in all cases.